Abnormal morphology biases haematocrit distribution in tumour vasculature and contributes to heterogeneity in tissue oxygenation

Miguel O. Bernabeu[1,*], Jakub Köry[2,3], James A. Grogan[2,3], Bostjan Markelc[4,5,3], Albert Beardo Ricol[1], Mayeul d'Avezac[6], Jakob Kaeppler[4], Nicholas Daly[1], James Hetherington[7,8], Timm Krüger[9], Philip K. Maini[2], Joe M. Pitt-Francis[10], Ruth J. Muschel[4], Tomás Alarcón[11,12], and Helen M. Byrne[2,12,*]

[1]Centre for Medical Informatics, Usher Institute, The University of Edinburgh, Edinburgh, UK
[2]Mathematical Institute, University of Oxford, Oxford, UK
[3]Equally contributing authors
[4]Department of Oncology, University of Oxford, Oxford, UK
[5]Department of Experimental Oncology, Institute of Oncology, Ljubljana, Slovenia
[6]Research Software Development Group, Research IT Services, University College London, London, UK
[7]The Alan Turing Institute, London, UK
[8]Department of Computer Science, University College London, London, UK
[9]School of Engineering, Institute for Multiscale Thermofluids, The University of Edinburgh, Edinburgh, UK
[10]Department of Computer Science, University of Oxford, Oxford, UK
[11]Centre de Recerca Matemàtica, Barcelona, Spain
[12]Equally contributing senior authors
[*]Corresponding authors: miguel.bernabeu@ed.ac.uk, helen.byrne@maths.ox.ac.uk

May 15, 2019

1

Abstract

Heterogeneity in oxygen distribution in solid tumours is recognised as a limiting factor for therapeutic efficacy. Vessel normalisation strategies, aimed at rescuing abnormal tumour vascular phenotypes and alleviating hypoxia, have become an established therapeutic strategy. However, understanding of how pathological blood vessel networks and oxygen transport are related remains limited. In this paper, we establish a causal relationship between the abnormal vasculature of tumours and their heterogeneous tissue oxygenation. We obtain average vessel lengths $\bar{L}$ and diameters $\bar{d}$ from tumour allografts of three cancer cell lines and observe a substantial reduction in the ratio $\lambda = \bar{L}/\bar{d}$ compared to physiological conditions. Mathematical modelling reveals that small values of the measured ratio λ (*i.e.* $\lambda < 6$) can bias haematocrit distribution in tumour vascular networks and drive highly heterogeneous tumour tissue oxygenation. Finally, we show an increase in the average λ value of tumour vascular networks following treatment with the DC101 anti-angiogenic cancer agent. Based on our findings, we propose a new oxygen normalisation mechanism associated with an increase in λ following treatment with anti-angiogenic drugs.

1   Introduction

Tissue oxygenation plays a crucial role in the growth and response to treatment of cancer. Indeed, well-oxygenated tumour regions respond to radiotherapy better than hypoxic or oxygen-deficient regions, by up to a factor of three [1, 2]. Further, the increased rates of proteomic and genomic modifications and clonal selection associated with anoxia (i.e., total oxygen depletion), endow tumours with more aggressive and metastatic phenotypes [3, 4]. Heterogeneous oxygen distributions in solid tumours are commonly attributed to their abnormal vasculature [5, 6]. While vessel normalisation strategies, aimed at reducing tumour hypoxia [7], have been shown to improve survival in *e.g.* glioblastoma patients undergoing chemotherapy and/or radiotherapy [8], the identification of patients who will benefit from such combined treatments remains an open question [3].

Detailed, functional imaging of the tumour microenvironment would enable the development of patient-specific treatment plans [9]. However, the maximum spatial resolution for imaging hypoxia via Positron Emission Tomography (PET) is currently 3–5 millimetres [10]. This resolution is three orders of magnitude larger than the micrometre scale governing oxygen transport in tissue and cell responses to hypoxia [11]. Consequently, PET images effectively mask intratumoural heterogeneity [10], which can lead to poor outcomes and foster the emergence of resistant clones [12]. A mechanistic understanding linking abnormal tumour vascular structure at the micrometre scale and oxygen heterogeneity at the tissue-scale is currently lacking. In this paper, we show how a multidisciplinary approach, which combines imaging with mathematical and computational modelling can be used to close this resolution gap [11, 13].

Oxygen is transported through the vasculature by binding to haemoglobin in red blood cells (RBCs) [13]. Haematocrit, or the volume fraction of RBCs in whole blood, does not distribute uniformly at vessel bifurcations (*i.e.* branching points where three vessels meet) [14, 15]. At a bifurcation with one afferent and two efferent branches, it is typically assumed that the efferent branch with the highest flow rate will have the

highest haematocrit [15, 16] due to, among other features, plasma-skimming caused by the presence of a RBC-depleted layer or cell free layer (CFL) [17]. Several theoretical models have been proposed to describe this effect *e.g.* [16, 18, 19]. Tumour vasculature is characterised by abnormal branching patterns, reduced average vessel lengths, and increased formation of arterio-venous shunts (see [20] for a review). While these changes can impact haematocrit splitting (HS), and tumour oxygenation, they have received little attention in the literature.

In this paper, we establish a causal relationship between the abnormal vasculature of tumours and their heterogeneous tissue oxygenation. When we extract average vessel lengths $\bar{L}$ and diameters $\bar{d}$ from tumour allografts of three cancer cell lines we observe a substantial reduction in $\lambda = \bar{L}/\bar{d}$ compared to physiological conditions. Detailed numerical simulations describing the transport of RBCs in plasma reveal that the average measured λ value in the tumour allografts is too small for the CFL to recover full symmetry between consecutive branching points. Further, the resulting bias in haematocrit distribution propagates and amplifies across multiple branching points. We argue that this memory effect can explain observations of haemo-concentration/dilution in tumour vasculature [21] and well perfused vessels that are hypoxic [22].

Based on the RBC simulations, we propose a new haematocrit splitting rule that accounts for CFL disruption due to pathologically small λ values. We integrate this rule into existing models of tumour blood flow and oxygen transport [23] and observe a haematocrit memory effect in densely branched vessel networks. The predicted tissue oxygenation is highly heterogeneous and differs markedly from predictions generated using rules for haematocrit splitting specialised for healthy vessel networks (*e.g.* [24, 25, 26, 5, 27]). Finally, we show an increase in the average λ value of tumour vascular networks following treatment with the DC101 anti-angiogenic cancer agent. Based on our results, we postulate the existence of a previously unreported tumour oxygen normalisation mechanism associated with an increase in the λ value after treatment with anti-angiogenic drugs.

2 Results

2.1 Distance between vascular branching points is on average shorter in solid tumours than in healthy tissue

We implemented a protocol for *in vivo* imaging of tumour vasculature [28] and exploited our recently published methods for vessel segmentation [29, 30] and three-dimensional (3D) vascular network reconstruction to characterise the morphology of tumour vasculature (see Methods section for more details). Briefly, tumour allografts of three murine cancer cell lines (*i.e.* MC38, colorectal carcinoma; B16F10, melanoma; and LLC, Lewis lung carcinoma) were implanted in mice, controlled for size, and imaged through an abdominal window chamber using a multi-photon microscope over multiple days. The vascular networks in the 3D image stacks were segmented and the associated network skeletons and vessel diameters computed [29, 30]. Figure 1(a) shows the two-dimensional (2D) maximum projection of an example network dataset along with a 2D projection of its segmentation and a close-in overlaying segmentation and skeletonisation. Vessel lengths (L) and diameters (d) in the networks followed a right-skewed distribution re-

(a) Multiphoton maximum intensity projection from MC38 dataset, network segmentation, and skeletonisation.

(b) Vessel length vs diameter from MC38 dataset

(c) Vessel length vs diameter from B16F10 dataset

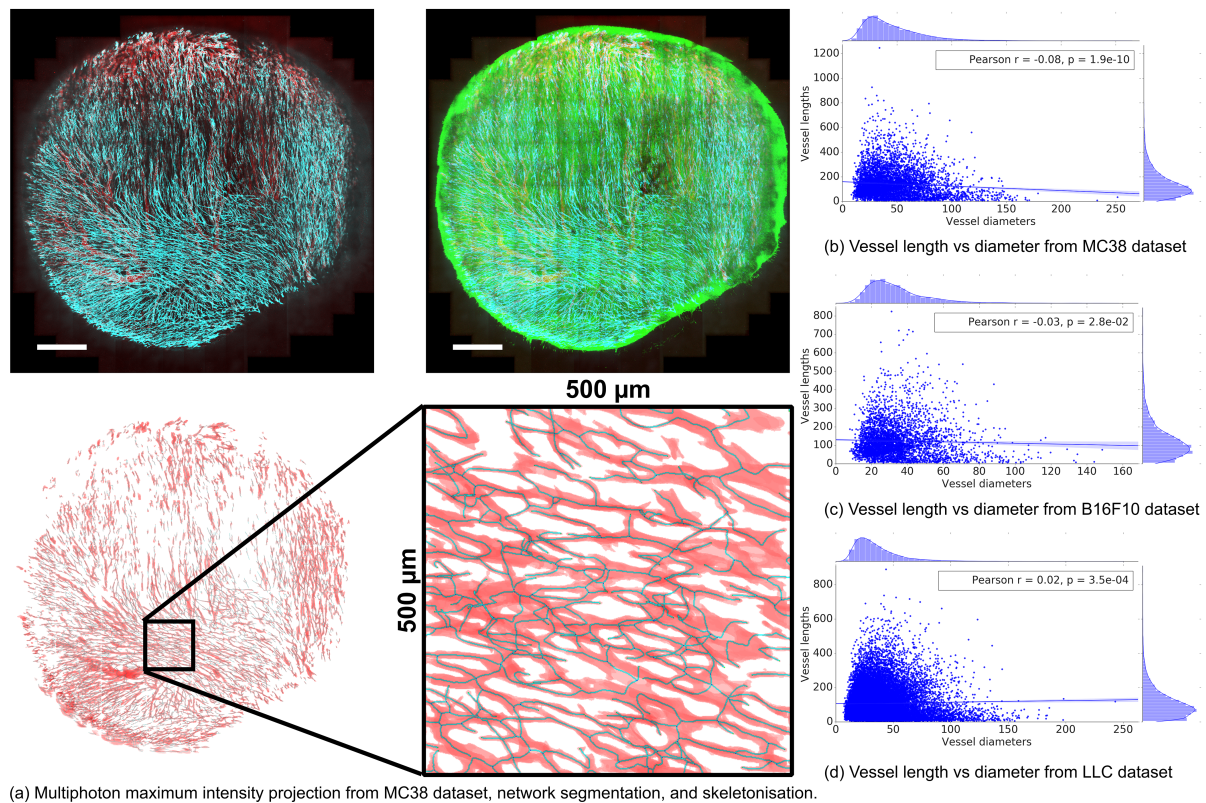(d) Vessel length vs diameter from LLC dataset

Figure 1: a) Maximum intensity projection of multiphoton image stack of a tumour vessel network obtained via an abdominal imaging window in mouse. Red - perfusion, Cyan - endothelial cells, Green - GFP tumor cells. Scale bar: 1 mm. The stack is subsequently segmented and skeletonised and distributions of vessel diameters and lengths are calculated. Mouse MC38-5 in Table 1. Scatter plots of vessel lengths versus diameters for different cell lines studied: b) MC38 (Mouse 3 in Table 1), c) B16F10 (Mouse 1 in Table 1), d) LLC (Mouse 1 in Table 1).

sembling a log-normal distribution (Figure 1(b)-(d)). No correlation was found between the variables (Pearson's $r^2 < 0.04$ for all samples analysed, Figure 1(b)-(d), Supplementary Tables S2–S3).

Table 1 summarises last-day statistics for all the experiments and averages per cell line. In the example MC38 dataset from Figure 1(a), average vessel length ($\bar{L}$) and diameter ($\bar{d}$) were 143 μm and 45.5 μm, respectively We observe how the group average vessel length is 128.6 μm, 125.9 μm, 108.8 μm for MC38, B16F10, and LLC, respectively. The average diameters are 33 μm, 36.5 μm, 35.7 μm, respectively, which is within the range previously described for tumour vasculature [31]. In addition, the length-to-diameter ratios (λ) are $4.0, 3.4, 3.0$, respectively, which is substantially smaller than typical λ values reported under physiological conditions in a variety of tissues (Table 2) and representative of the high branching density encountered in tumour vasculature [20].

4

Table 1: Mean branch lengths ($\bar{L}$), mean vessel diameters ($\bar{d}$), and length-to-diameter ratio ($\lambda = \frac{\bar{L}}{\bar{d}} = \frac{\sum L_i}{\sum d_i}$) measured in mouse for different tumour models over all the vessels imaged. See Supplementary Tables S2–S3 for correlation between variables.

Cell line	MC38						
Mouse	1	2	3	4	5	6	Av.
$\bar{L}, \mu$m	123.9	129.9	143	112.4	132.1	130.0	128.6
$\bar{d}, \mu$m	29.3	33.0	45.5	23.9	28.9	37.5	33.0
$\lambda = \bar{L}/\bar{d}$	4.2	3.9	3.1	4.7	4.6	3.4	4.0

Cell line	B16F10				LLC
Mouse	1	2	3	Av.	1
$\bar{L}, \mu$m	123.2	123.5	131.0	125.9	108.8
$\bar{d}, \mu$m	33.9	34.1	41.6	36.5	35.7
$\lambda = \bar{L}/\bar{d}$	3.6	3.6	3.1	3.4	3.0

Table 2: Average vessel length and diameter reported under physiological conditions in a variety of tissues.

Animal (tissue)	Vessel type	$\bar{d}(\mu$m)	$\bar{L}(\mu$m)	$\lambda = \bar{L}/\bar{d}$	Reference
Wistar Kyoto Rat (mesentery)	Arteriole	13.2	337.0	25.5	[32, 33]
	Capillary	8.7	424.0	48.7	[32, 33]
	Venule	20.6	334.0	16.2	[32, 33]
Myotis Bat (wing)	Arteriole	7.0	206.0	29.4	[34]
	Capillary	3.7	74.0	20.0	[35]
	Venule	21.0	200.0	9.5	[35]
Cat (sartorius muscle)	Arteriole	7.4	96.0	13.0	[36]
	Venule	6.8	68.0	10.0	[37]
Golden Hamster (retractor muscle)	Arteriole	5.7	101.2	17.8	[38]
	Venule	3.6	57.7	16.0	[38]
Human	Capillary	5.0	350.0	70.0	[39]

2.2 Plasma skimming in tumour-like vasculature is biased by history effects arising from CFL dynamics

Our finding of reduced inter branching point distance in tumour tissue motivated us to investigate a potential causal relationship between the reduction in L and λ and the profoundly abnormal tumour haemodynamics and mass transport patterns described in the literature [40]. In particular, we are interested in unravelling potential haemorheological phenomena contributing to tumour heterogeneity and hypoxia.

The presence of a RBC-depleted region adjacent to the vessel walls (*i.e.* the cell free layer (CFL)) is a key contributor to plasma skimming (PS) [15, 16, 17]. Previous studies have shown CFL disruption after microvascular bifurcations and found that the length required for CFL recovery is in the region of 10 vessel diameters (d) for $d < 40\mu$m [16], $8 - 15d$ for $d \in [20, 24]\mu$m [41], and $25d$ for $d \in [10, 100]\mu$m [42]. These values are substantially higher than the average λ values given in Table 1 and therefore we expect that, on average, CFL symmetry will not recover between the branching points in the networks under study.

Motivated by these findings, we exploited recent advances in blood flow simulation methods [43] to investigate the link between CFL dynamics and PS in a tumour-inspired microvascular network. Our intention is to understand whether CFL disruption effects arising at any given bifurcation can affect haematocrit splitting in downstream bifurcations for small inter-bifurcation distances relevant to tumour vasculature (see Methods section for further details). Briefly, we define a set of networks of cylindrical channels of constant radius, consisting of one main channel with an inlet and an outlet at either side and two side branches, which effectively define two consecutive bifurcations (Supplementary Figure S1). We consider inter-bifurcation distances of four and 25 channel diameters based on our tumour vascular network analysis and the largest of the CFL recovery distances reviewed earlier. We position the two side branches on the same side of the main channel or on opposite sides. A computational model of liquid-filled deformable particles (discocytes approximating the shape of an RBC) suspended in an ambient fluid is used to simulate blood flow in the networks, with RBCs inserted at the network inlet and removed at the outlets (see Section 4 and Supplementary Material for a summary of the simulation parameters). Flow rates at the inlets and the outlets of the network are configured such that at each bifurcation flow is split evenly. We perform blood flow simulations (3 runs in each network, with random perturbations in the RBC insertion procedure) and, after the initial transient required to fully populate the network with RBCs, we quantify haematocrit by an RBC-counting procedure.

Figure 2a–2b and Table 3 show how haematocrit split is close to even at bifurcation 1 for all geometries studied, as would be predicted by existing HS theoretical models. However, different degrees of haematocrit splitting occur at bifurcation 2. In the double-t geometry, we observe haemodilution in branch 3 and haemoconcentration in branch 4 (16.8% vs 23%, $p < 0.001$, Figure 2b). We will refer to these as the unfavourable and favourable branches. These effects are no longer statistically significant in the same branches in the extended double-t geometry (19.1% vs 19.4%, $p = 0.3$, Figure 2a). The haemoconcentration/haemodilution effect is also present in the cross geometry but the branches experiencing it are interchanged (22.1% vs 17.1%, $p < 0.001$, Figure 2c). In contrast with these results, existing HS theoretical models would predict even haematocrit

Table 3: Haematocrit calculated at the different branches of each bifurcation for the extended double-t (EDT) geometry, double-t (DT) geometry, and cross (X) geometry. Values are given as mean (standard error) over an ensemble of three simulations with random perturbations in the RBC insertion procedure while the haematocrit at the inlet is held constant.

| | Bifurcation 1 | | | Bifurcation 2 | | |
	Branch 0	Branch 1	Branch 2	Branch 1	Branch 3	Branch 4
EDT	20.06(0.03)	19.23(0.14)	20.8(0.1)	19.23(0.14)	19.05(0.22)	19.4(0.23)
DT	20.08(0.06)	19.96(0.19)	20.26(0.05)	19.96(0.19)	16.83(0.24)	23.04(0.46)
X	20.06(0.02)	19.67(0.09)	20.35(0.2)	19.67(0.09)	22.12(0.26)	17.09(0.13)

splitting at bifurcation 2, regardless of the inter-bifurcation distance, due to the prescribed symmetrical flow and geometry conditions.

On closer inspection, the dynamics of the CFL show how, after bifurcation 1, CFL width is initially negligible and rapidly increases on the side of channel 1 leading to the favourable branch ($\theta = 0$, Figure 2f). Conversely, CFL width increases after the bifurcation and follows a downward trend in the opposite side ($\theta = \pi$, Figure 2f). An inter-bifurcation distance of four diameters is not sufficient for the CFL width to equalise on both sides (Figures 2f). In contrast, CFL width has time to become symmetric on both sides for an inter-bifurcation distance of 25 diameters (Figure 2g).

Taken together, these results show how CFL asymmetry can cause uneven haematocrit split in bifurcation 2 (Figure 2e). Our results are consistent with the findings by Pries *et al.*, describing how asymmetry of the haematocrit profile in the feeding vessel of a bifurcation has a significant influence on RBC distribution in the daughter vessels [16]. In addition, we provide quantitative evidence of how CFL asymmetry may be the main contributing factor.

Interestingly, we observe small but statistically significant asymmetries in the haematocrit split in bifurcation 1 in the extended double-t geometry (19.2% vs 20.8%, $p < 0.001$, Figure 2a) and cross geometry (19.7% vs 20.4%, $p = 0.035$, Figure 2c), which consistently favour the side branch. We attribute this secondary effect to an asymmetrical streamline split in the chosen geometry as investigated in [44].

We note that the effects described above depend on the angle defined by the planes containing the two consecutive bifurcations. Our data suggest that for an angle of $\frac{\pi}{2}$ radian the favourable/unfavourable effects will not be observed (Supplementary Figure S2).

2.3 Haematocrit history effects lead to highly heterogeneous oxygen distribution in solid tumours

Existing theoretical models of HS [45, 19, 46] do not reproduce the haemoconcentration/haemodilution effects in the previous section. We hypothesise that this is because they neglect CFL disruption at bifurcations and its impact on subsequent bifurcations. We propose a new haematocrit splitting (HS) model which accounts for CFL dynamics and show that it predicts history effects in dense networks (see the Methods section for details and Supplementary Material for a description of its validation using the results
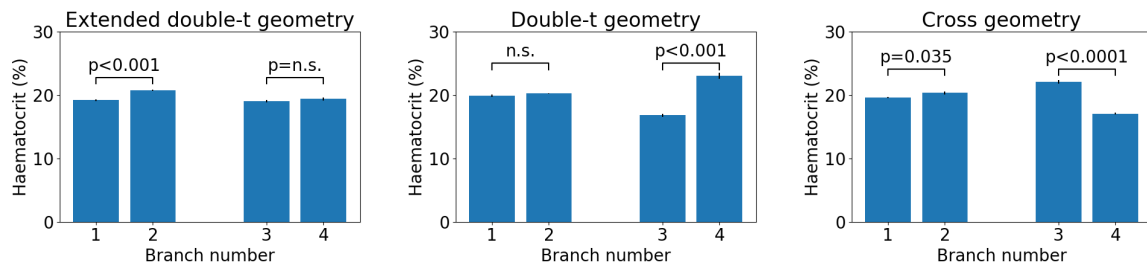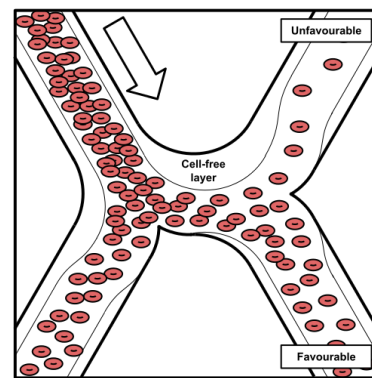
(a) Extended double-t geometry (see Suppl. Fig. S1a)

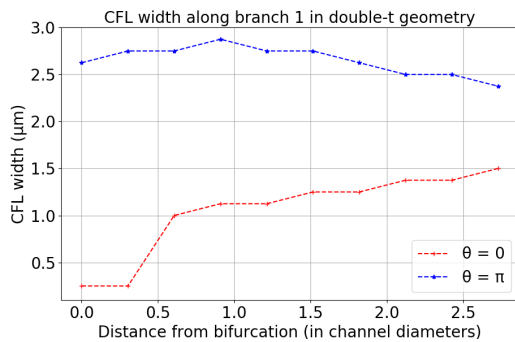(b) Double-t geometry (see Suppl. Fig. S1b)
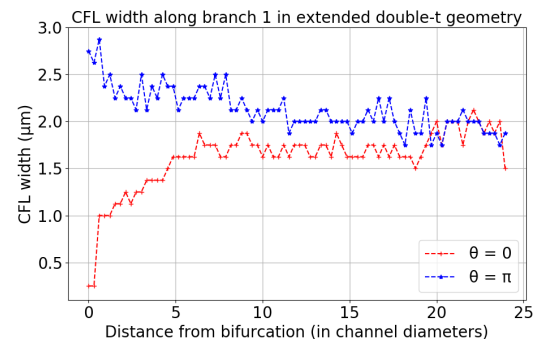
(c) Cross geometry (see Suppl. Fig. S1c)
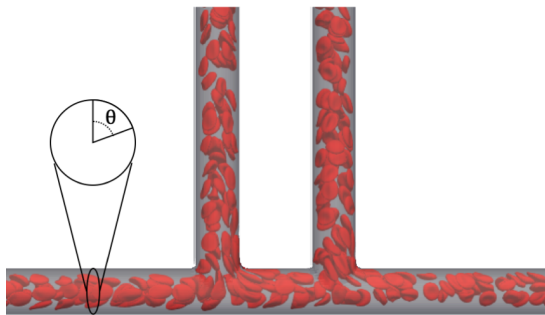
(d) Simulated RBCs in domain.

(e) Illustration of CFL dynamics and plasma skimming.

(f) CFL branch 1 (double-t geometry)

(g) CFL branch 1 (extended double-t geometry)

Figure 2: Haematocrit at different geometry branches (see Supplementary Figure S1 for geometry schematics): a) extended double-t geometry, b) double-t geometry, c) cross geometry. Example simulation in the double-t geometry: d) vessel network is rendered semi-transparent in grey, RBC membranes are rendered in red suspended in transparent blood plasma. e) Schematic describing the impact of CFL dynamics on haematocrit split. CFL width in opposite sides of channel 1: f) double-t geometry, g) extended double-t geometry.

8

from Section 2.2). Computationally, the new model is significantly less expensive than the RBC simulations.

We use Murray's law [47] and our experimentally measured values of λ to design an idealised vessel network (see Supplementary Figure S4a and Methods section for details). Most notably we choose equal flow split and radii in daughter branches of any bifurcation, a scenario where existing HS models would predict homogeneous haematocrit throughout the network. We simulate network blood flow using a Poiseuille flow approximation with a HS model originally proposed by Pries *et al.* [16, 45] (without memory effects) and our new model (accounting for memory effects). As for the RBC simulations, differences in haematocrit between daughter branches emerge after two bifurcations (Supplementary Figure S4c), and are amplified with increasing vessel generation number (Supplementary Figure S4d). By contrast, existing models predict uniform splitting of the flow and haematocrit if the daughter vessels have equal radii (Supplementary Figure S4d).

Our model predicts the emergence of a compensatory mechanism in daughter branches. Increased flow resistance in the branch experiencing haemoconcentration leads to partial re-routing of flow in the other branch (Supplementary Figure S4b). This, in turn, attenuates the haemoconcentration/haemodilution effects described in Section 2.2 due to HS dependence on flow ratios.

We now consider how this memory effect in the haematocrit distribution may affect oxygen distribution in the tissue being perfused by the network. Following [23] (see Methods section for a description of the coupled model), the calculated haematocrit distribution in the synthetic network acts as a distributed source term in a reaction-diffusion equation for tissue oxygen. We define sink terms so that oxygen is consumed at a constant rate everywhere within the tissue. The equation is solved numerically and oxygen distributions generated using the two HS models (with and without memory effects) are compared for a range of λ values. The results presented in Figure 3c and Supplementary Figure S5 show that for larger values of λ the differences in the oxygen distribution in the tissue for the two haematocrit splitting models are not statistically significant ($\lambda = 10$, $p = 0.14$). However, as λ decreases, statistically significant differences appear (for example, with $\lambda = 4$, $p < 0.001$). Without memory effects, the oxygen distributions become more focussed as λ decreases; with memory effects, the oxygen distributions are flatter for all values of λ. A similar trend is observed for moderate values of λ but the distributions are significantly more diffuse (see Supplementary Figure S5c).

2.4 Vascular normalisation therapies increase lambda ratio in tumours

Our findings of reduced λ ratio in tumour vasculature and associated predictions of increased oxygen heterogeneity led us to investigate whether existing vascular normalisation therapies modulate this parameter. Previous reports (Table 4) have extensively demonstrated in multiple animal models that anti-angiogenic treatment leads to reduction in tumour vessel diameters. In those studies that analyse vessel length and diameter post-treatment, vessel length either remains unchanged or decreases to a lesser extent than vessel diameter. These findings indicate an increase in lambda ratio post-treatment. Furthermore, Kamoun *et al.* also reported a reduction in tumour haemoconcentration

9
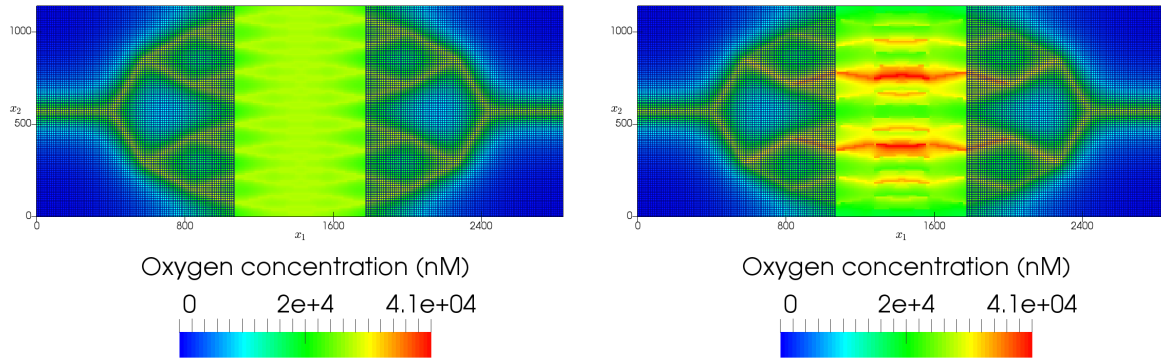
(a) $\lambda = 4$, model without memory effects

(b) $\lambda = 4$, model with memory effects
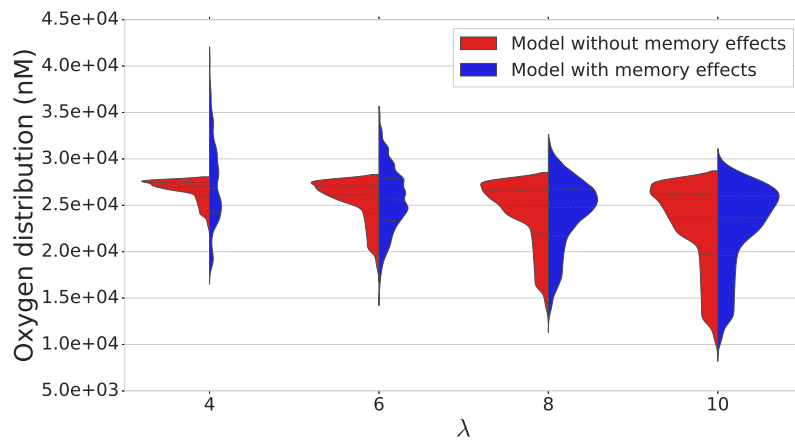
(c) Tissue oxygen concentration distributions for varying λ

Figure 3: For $\lambda = 4.0$, the model with memory effects clearly yields more heterogeneity, especially in the region of interest, as highlighted in (a) and (b) (note that the spatial scales are in microns). Violin plots in (c) show oxygen distributions for varying λ and the two models under consideration. Heterogeneity increases with λ for the model without memory effects as expected, but the model with memory effects predicts increased heterogeneity for very low λ. The horizontal lines in oxygen distributions in (c) represent 25, 50 and 75% percentiles.
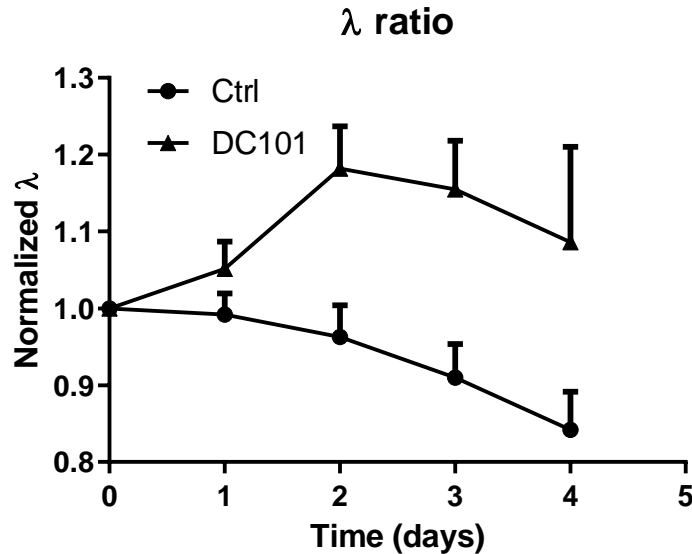
10

Figure 4: λ ratio in MC38 tumours over time following DC101 treatment compared with control (n=5). DC101 raw data is given in Supplementary Table S1.

post-treatement [48], which suggests an *in vivo* link between an increase in λ, haematocrit normalisation and oxygen transport homogenisation.

We validated these results in our animal model by calculating the λ ratio following DC101 treatment. Our results indicate that in the first two days post-treatment λ increases significantly and then decreases to match the control trend (Figure 4, Supplementary Table S1). This change is explained by a linear increase in vessel length immediately after treatment (absent in the control group), which is compensated after two days by an increase at a higher rate in vessel diameter (comparable to the control group) (Supplementary Figure S6).

3 Discussion

Hypoxia compromises the response of many tumours to treatments such as radiotherapy, chemotherapy and immunotherapy. Dominant causative factors for hypoxia associated with the structure and function of the tumour vasculature include tortuosity, immature blood vessels that are prone to collapse, and inadequate flow regulation. Motivated by morphological analyses of vascular networks from different tumour types and detailed computer simulations of RBC transport through synthetic networks, we have proposed a new, rheological mechanism for tumour hypoxia.

We analysed vascular networks from murine MC38, B16F10, and LLC tumour allografts. For each vessel segment within each network, we calculated a novel metric λ which is the ratio of its length and diameter. Average λ values for the three tumour cell lines were similar in magnitude ($\lambda \in [3, 4.2]$) and several fold smaller than values from a range of healthy tissues ($\lambda \in [9.5, 70]$).' Detailed numerical simulations of RBC transport in plasma confirmed previous reports of transient alterations in the CFL downstream

11

Table 4: Previous studies reporting morphological or haemodynamic changes following vascular normalisation therapy.

Ref.	Model	Treatment	Changes reported	λ ratio implications	Efficacy
[49]	MDA-MB-361HK tumour model	Herceptin	Reduced vessel diameter, unchanged length	λ increase	Tumour growth slowed and increased survival
[50]	Shionogi tumour model	Androgen withdrawal	Reduced vessel diameter	Possible λ increase	Tumour regression followed by relapse
[48]	Glioblastoma tumour model	Cediranib	Transient reduction in vessel diameter and haemoconcentration	Possible λ increase	Increased survival
[51]	Rip-Tag2 tumour model	Anti-α6 integrin antibody	Reduced vessel diameter	Possible λ increase	Impaired tumour angiogenesis
[52]	Murine mammary carcinoma MCaIV	DC101	Relatively higher reduction in diameter than in length	λ increase	Increased drug penetration via functional normalisation
[53]	LS174T tumour model	Anti-VGF antibody (A4.6.1)	Reduced vessel diameter, unchanged length	λ increase	Vascular regression and decreased permeability

12

of network bifurcations (*e.g.* asymmetries in the cross-sectional haematocrit profile following a bifurcation [54] and the temporal dynamics governing its axisymmetry recovery [42]). Further, for the λ values measured in our tumours and the capillary number considered in our simulations, the CFL did not become symmetric between consecutive branching points. This bias is amplified across branching points and drives haemoconcentration/haemodilution at the network level. Based on these findings, we developed a new rule for haematocrit splitting at vessel bifurcations that accounts for CFL disruption due to abnormally short vessel segments. We then used our existing computational software [23] to demonstrate that this haematocrit memory effect can generate heterogeneous oxygen distributions in tissues perfused by highly branched vascular networks and that the network metric λ controls the extent of this heterogeneity. Finally, we reported an increase in the average λ value of tumour vascular networks following treatment with the DC101 anti-angiogenic cancer agent.

The implications of our findings are multiple. We have introduced a simple metric to characterise tumour vasculature based on the mean length-to-diameter ratio of vessel segments ($= \lambda$), and demonstrated how it can generate oxygen heterogeneity in an idealised, densely vascularised, tissue model. Our findings, of structurally induced haemodilution in vascular networks with low λ values, provide a mechanistic explanation for experimental observations of haemodilution in tumour vascular networks [21], the existence of well-perfused vessels that are hypoxic [22], and a possible explanation for the presence of cycling hypoxia in tumour microenvironment [55]. We conclude that vessel perfusion is a poor surrogate for oxygenation in tissue perfused by vascular networks with low λ values. Further, predictions of tissue oxygenation based on diffusion-dominated oxygen transport (*e.g.* [24, 25, 26, 5, 27]) may be inaccurate if they neglect heterogeneity in the haematocrit distribution of the vessel network. One way to address the resolution gap in current imaging modalities is to leverage mathematical modelling to infer micrometre scale information about oxygen levels from tissue scale images [11]. Such a theoretical framework must account for the complex interplay between microvascular structure, blood rheology, and oxygen transport, as highlighted in the current work.

Finally, anti-angiogenic drugs have been shown to generate transient periods of heightened homogeneous tissue oxygenation, due to improved restructuring and reduced permeability of tumour vessels [52]. This phenomenon, termed 'vascular normalisation' [6], can correct the deficient transport capabilities of tumour vasculature, homogenise drug and oxygen coverage, and, thereby, improve radiotherapy and chemotherapy effectiveness [2]. Based on our findings, we postulate the existence of a previously unreported oxygen normalisation mechanism associated with an increase in the average λ value of tumour vascular networks post treatment with anti-angiogenic drugs. Our results demonstrate how such morphological changes would lead to a less heterogeneous haematocrit distribution and more uniform intratumoural oxygenation. Further experimental work, measuring haematocrit before and after anti-angiogenic treatment, is needed to test this hypothesis and elucidate its importance in comparison with established mechanisms of normalisation (*e.g.* permeability reduction, vessel decompression [56]). If confirmed, this finding would provide a theoretical foundation for the development of therapeutic approaches for the normalisation of tumour oxygenation involving the administration of vascular targeting agents that normalise λ and, therefore, homogenise haematocrit and tissue oxygenation. Possible mechanisms to be targeted would include, among others, the

promotion of post-angiogenic vascular remodelling [57, 58, 59], in particular vessel pruning and diameter control, or the modulation of currently unexplored temporal regulators of vascular patterning [60].

In summary, tissue oxygenation is central to cancer therapy. Understanding what controls tumour tissue oxygen concentration and transport properties is key to improving the efficacy of cancer treatments based on new and existing methods. Unravelling the causal relationship between vessel network structure and tissue oxygenation will pave the way for new therapies.

4   Methods

4.1   Tumour allograft model and abdominal imaging window protocol

We used an abdominal window chamber model in mice, which allowed for intravital imaging of the tumors [28]. The abdominal window chamber was surgically implanted in transgenic mice on C57Bl/6 background that had expression of red fluorescent protein tdTomato only in endothelial cells. The murine colon adenocarcinoma - MC38, murine melanoma - B16F10, and murine Lewis Lung Carcinoma – LLC tumors with expression of green fluorescent protein (GFP) in the cytoplasm were induced by injecting 5 μl of dense cell suspension in a 50/50 mixture of saline and matrigel (Corning, NY, USA). For DC101 treatment, mice bearing MC38 tumors were treated with anti-mouse VEGFR2 antibody (clone DC101, 500 μg/dose, 27 mg/kg, BioXCell) injected intraperitoneally on the first and fourth day of imaging. Prior to imaging we intravenously injected 100 μl of Qtracker 705 Vascular Labels (Thermo Fisher Scientific, MA, USA) which is a blood-pool based labelling agent, thus allowing us to determine whether vessels were perfused or not. Isoflurane inhalation anesthesia was used throughout the imaging, mice were kept on a heated stage and in a heated chamber and their breathing rate was monitored. Tumor images were acquired with Zeiss LSM 880 microscope (Carl Zeiss AG), connected to a Mai-Tai tunable laser (Newport Spectra Physics). We used an excitation wavelength of 940 nm and the emitted light was collected with Gallium Arsenide Phosphide (GaAsP) detectors through a 524–546 nm bandpass filter for GFP and a 562.5–587.5 nm bandpass filter for tdTomato and with a multi-alkali PMT detector through a 670–760 bandpass filter for Qtracker 705. A 20x water immersion objective with NA of 1.0 was used to acquire a Zstacks-TileScan with dimensions of 512x512 pixels in x and y, and approximately 70 planes in z. Voxel size was 5 μm in the z direction and 0.83 μm x 0.83 μm in the x-y plane. Each tumor was covered by approximately 100 tiles. The morphological characteristics of tumor vasculature were obtained from the acquired images as previously described [29, 30]. All animal studies were performed in accordance with the Animals Scientific Procedures Act of 1986 (UK) and Committee on the Ethics of Animal Experiments of the University of Oxford.

4.2   RBC simulations in synthetic capillary networks

We define a set of networks of cylindrical channels of diameter d. An inlet channel of length $25d$ (channel 0) bifurcates into two channels of length δ and $25d$ at π and

14

Table 5: Parameters in blood flow simulations

Parameter	Description	Value	Reference
d	Cylindrical channel diameter	$33~\mu$m	Own results
L'	Inlet/outlet channel length	$25d$	[42]
δ	distance between branching points	$4d, 25d$	[42], Own results
$\bar{v}_{inlet}$	inlet mean velocity	$600~\mu$m/s	[21]
H_{inlet}	inlet discharge haematocrit	20%	[21]

$\pi/2$ radians clockwise, respectively (channels 1 and 2). Channel 1 bifurcates into two channels of length $25d$ at π and α radians clockwise, respectively (channels 3 and 4). We consider the following configurations (Supplementary Figure S1): double-t geometry ($\delta = 4d, \alpha = \pi/2$), cross geometry ($\delta = 4d, \alpha = 3\pi/2$), and extended double-t geometry ($\delta = 25d, \alpha = \pi/2$).

A model of liquid-filled elastic membranes (discocytes of 8 μm diameter approximating the shape of an RBC) suspended in an ambient fluid is used to simulate blood flow in the networks. We use the fluid structure interaction (FSI) algorithm previously presented and validated by Krüger *et al.* [61], which is based on coupling the lattice Boltzmann method (LBM), finite element method (FEM), and immerse boundary method (IBM). The discocyte membranes are discretised into 500 triangles, which imposes a voxel size of 0.8μm on the regular grid used in the LBM simulation. The mechanical properties of the membrane are defined to achieve a capillary number (*i.e.* the ratio of viscous fluid stress acting on the membrane and a characteristic elastic membrane stress) of 0.1 in channel 0. The coupled algorithm is implemented in the HemeLB blood flow simulation software [62, 63] (http://ccs.chem.ucl.ac.uk/hemelb). Simulations ran on up to 456 cores of the ARCHER supercomputer taking 11–32 hours. See Supplementary Material A.2 for full details.

A constant flow rate of $Q_0 = \bar{v}_{inlet}\pi d^2/4$ and a procedure for RBC insertion with tube haematocrit H_{inlet} is imposed at the network inlet. The outlet flow rates are set to $Q_2 = Q_0/2$ and $Q_{3,4} = Q_0/4$ to ensure an equal flow split at each bifurcation. RBCs are removed from the computational domain when they reach the end of any outlet channel. Table 5 summarises the key model parameters in the model. We performed blood flow simulations (3 runs in each network, with random perturbations in the RBC insertion procedure) and, after the initial transient required to fully populate the network with RBCs, we quantified haematocrit by an RBC-counting procedure.

4.3 Hybrid model for tissue oxygen perfusion that accounts for history effects in vascular networks

We first explain how our vascular networks are designed. Then, we describe how blood flow and haematocrit are determined. Next, we introduce the HS models and explain how CFL memory effects are incorporated and the resulting flow problem solved. We conclude by describing how the resulting haematocrit distribution is used to calculate oxygen perfusion in the surrounding tissue. The basic steps of our method are summarised in the flow chart in Supplementary Figure S3.

15

4.3.1 Network design

Our networks have one inlet vessel (with imposed blood pressure and haematocrit; we call this generation 0), which splits into two daughter vessels (generation 1), which then split into two daughter vessels (generation 2), and so on until a prescribed (finite) number of generations is reached. Thereafter, the vessels converge symmetrically in pairs until a single outlet vessel is obtained (with imposed blood pressure). At every bifurcation, the diameters of the two daughter vessels are assumed to be equal and determined by appealing to Murray's law [47]. Using the same vessel diameters in all simulations, we vary vessel lengths, so that for all vessels in the network, the lengths equal the product of λ (which is fixed for a given network) and the vessel diameter. We focus on λ-values in the range measured in our tumours (see Section 2.1 and Supplementary Material).

4.3.2 Blood flow and haematocrit splitting

Network flow problem. Tissue oxygenation depends on the haematocrit distribution in the vessel network perfusing the tissue. The haematocrit distribution depends on the blood flow rates. These rates are determined by analogy with Ohm's law for electric circuits, with the resistance to flow depending on the local haematocrit via the Fahraeus-Lindquist effect (for details, see Supplementary Material and [64]). The flow rates and haematocrit are coupled. We impose conservation of RBCs at all network nodes[1]. A HS rule must then be imposed at all diverging bifurcations.

HS model without memory effects. The empirical HS model proposed by Pries *et al.* [65] states that the volume fraction of RBCs entering a particular branch FQ_E depends on the fraction of the total blood flow entering that branch FQ_B as follows:

$$\mathrm{logit}(FQ_E) = A + B\,\mathrm{logit}\left(\frac{FQ_B - X_0}{1 - 2X_0}\right), \qquad (1)$$

where $\mathrm{logit}(x) = \ln(x/(1-x))$, B serves to as a fitting parameter for the nonlinear relationship between FQ_E and FQ_B, and A introduces asymmetry between the daughter branches (note that for an equal flow split $FQ_B = 0.5$, $A \neq 0$ yields uneven splitting of haematocrit). Finally, X_0 is the minimum flow fraction needed for RBCs to enter a particular branch (for lower flow fractions, no RBCs will enter)[2]; the term $(1 - 2X_0)$ reflects the fact that the CFL exists in both daughter vessels (see Supplementary Figure S7a).

HS model with memory effects. We account for the effects of CFL disruption and recovery by modifying the parameters A and X_0 (as already observed in [16]). For simplicity, and in the absence of suitable data, we assume that the parameter B is the same in both daughter branches. If $X_{0,f}$ (A_f) and $X_{0,u}$ (A_u) denote the values of X_0

---

[1] $\sum_i \tilde{Q}_i H_i = 0$, where we sum over all vessels i meeting at a given node with haematocrit H_i and signed flow rates $\tilde{Q}_i$ (of magnitude Q_i).

[2] The dependences of A, B and X_0 on the diameters of the participating vessels and on the parent vessel haematocrit are described in Supplementary Material, see equations (S.14)-(S.16).

(A) in the favourable and unfavourable daughter branches (see Figure 2e), then our new model of HS can be written as:

$$\text{logit}(FQ_{E,f}) = A_f + B\,\text{logit}\left(\frac{FQ_{B,f} - X_{0,f}}{1 - X_{0,u} - X_{0,f}}\right),\tag{2}$$

where subscripts $_f$ and $_u$ relate to favourable and unfavourable branches, respectively (see Supplementary Figure S7a for a graphical depiction). It is possible to rewrite Equation (2) in terms of the suspension flow rates $Q \equiv Q_B$ and haematocrit levels H of the favourable f, unfavourable u, and parent P vessels as (for details see Supplementary Material):

$$\frac{H_f}{H_u} = e^{A_f} \times \left(\frac{Q_f - X_{0,f}Q_P}{Q_u - X_{0,u}Q_P}\right)^B \times \frac{Q_u}{Q_f}.\tag{3}$$

This formulation of our HS model facilitates comparison with other HS models [18, 19, 46]. Functional forms for A_f, $X_{0,f}$ and $X_{0,u}$ are based on our RBC simulation results and the existing literature (see Supplementary Material). We use an iterative scheme (as in [19]) to determine the flow rates and haematocrit in a given network.

4.3.3 Calculating the tissue oxygen distribution

We embed the vessel network (described in Section 4.3.1) in a rectangular tissue domain. A steady state reaction-diffusion equation models the tissue oxygen distribution, with source terms at vessel network locations proportional to the haematocrit there, and sink terms proportional to the local oxygen concentration modelling oxygen consumption by the tissue. This equation is solved numerically using Microvessel Chaste (see [23] and Supplementary Material for details). In order to highlight the influence of HS on tissue oxygen, we focus on the central 25% of the domain which is well-perfused and ignore the avascular corner regions (see Figures 3a and 3b)

Acknowledgments

(a) Extended double-t geometry
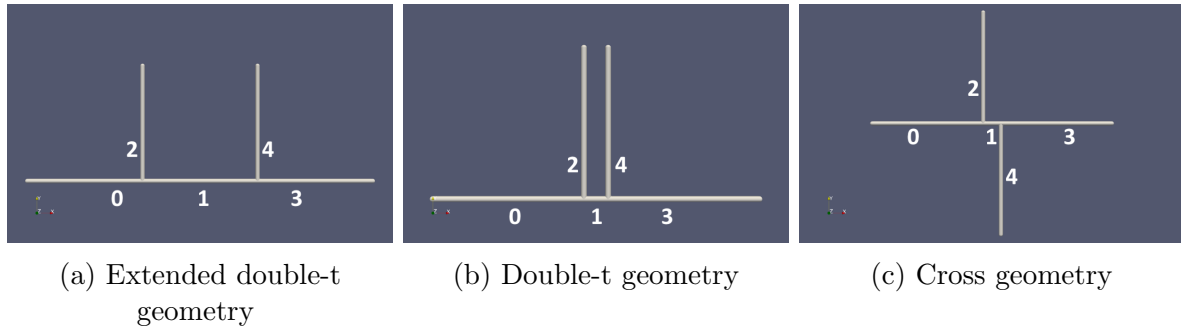
(b) Double-t geometry

(c) Cross geometry

Figure S1: Computational domains considered showing the numbering of the different channels in the network: a) extended double-t geometry, b) double-t geometry, c) cross geometry.
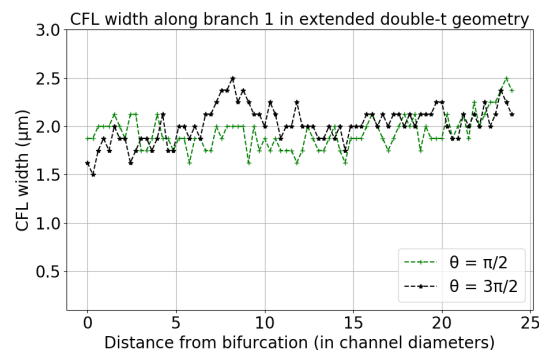

Figure S2: CFL channel 1 double-t geometry perpendicular to bifurcation planes.

A   Supplementary Material

The Supplementary material is organised as follows. In A.1, we provide experimental evidence which supports the hypothesis that vessel lengths and diameters are uncorrelated in tumour environments. We describe the FSI algorithm used for the RBC simulations in A.2 and the method used to calculate the width of the CFL in A.3. We present our hybrid model of tissue perfusion in A.4 and introduce our new HS model in A.5. In A.6, we comment on the higher mean oxygen values predicted by our oxygen perfusion model for small λ values.

Table S1: λ values measured in MC38 tumours following DC101 treatment over time.

Day	Mouse 1	Mouse 2	Mouse 3	Mouse 4	Mouse 5
0	4.532	4.065	4.141	4.122	4.054
1	5.301	4.098	4.336	4.432	3.878
2	6.222	4.429	4.396	5	4.756
3	5.382	4.465	3.89	5.353	5.068
4	4.395	4.418	3.273	6.342	4.237

Vessel network: blood flow and haematocrit

Start:
input λ
$(2 \leq \lambda \leq 20)$

Generate synthetic
vessel network

Solve haematocrit
and flow problems
using HS model
without memory

Solve haematocrit
and flow problems
using HS model
with memory

Define spatial
domain and
discretise it using
a regular grid

Embed vessel
network into
tissue domain

Solve reaction-
diffusion equation
to determine
tissue oxygen
distribution

Compare output
from the two
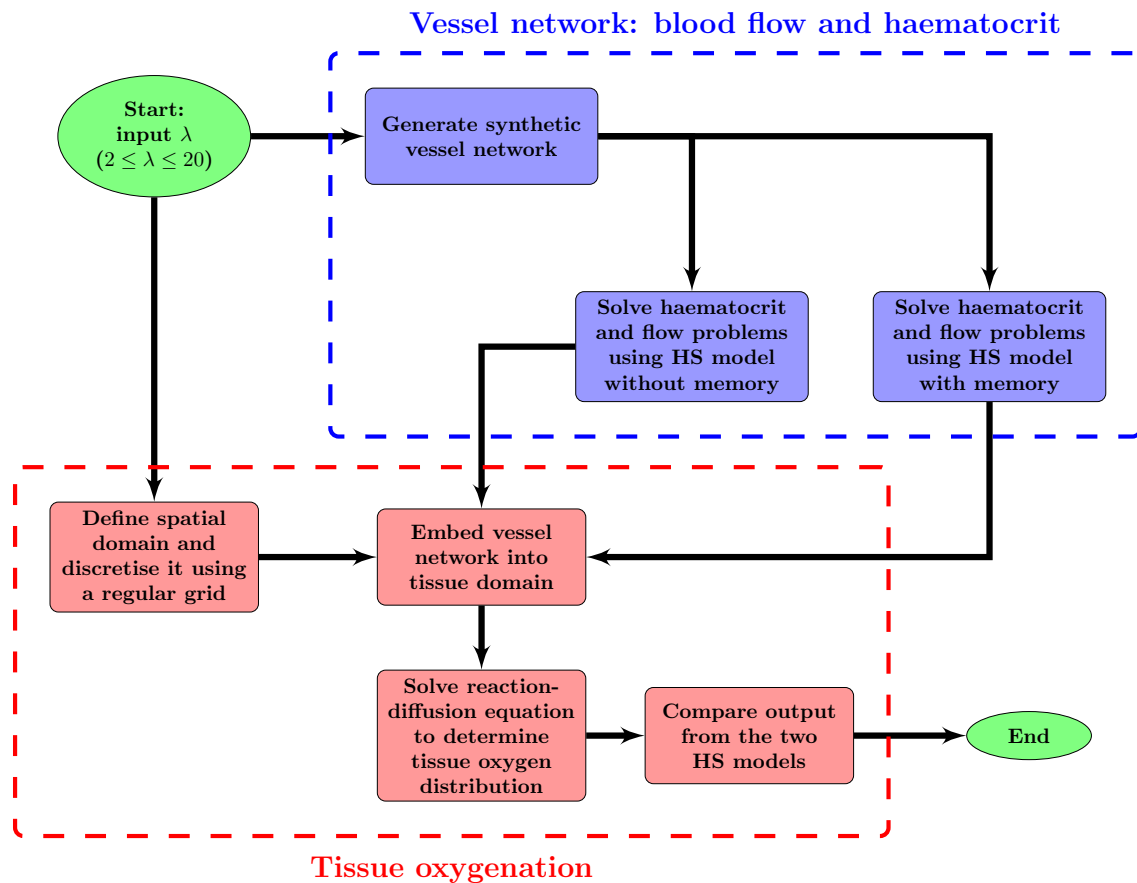HS models
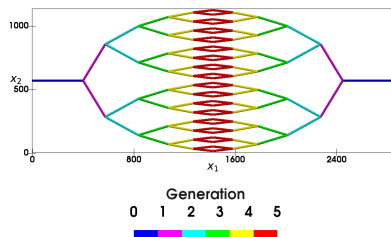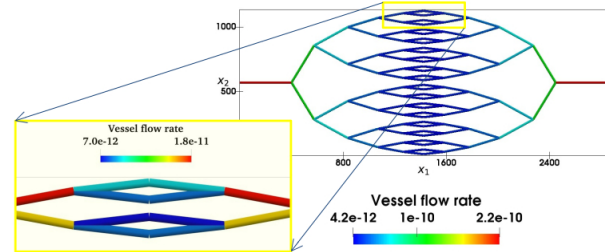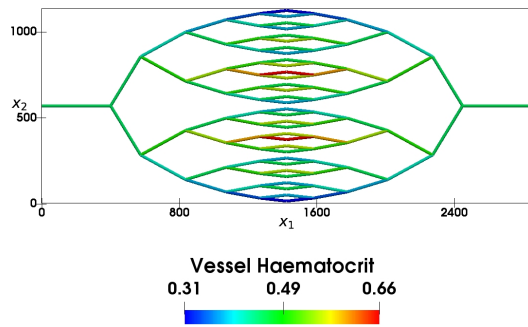
End

Tissue oxygenation

Figure S3: Flow chart summarising the main components of our hybrid model for tissue oxygen perfusion, as implemented within Microvessel Chaste (see [23]).
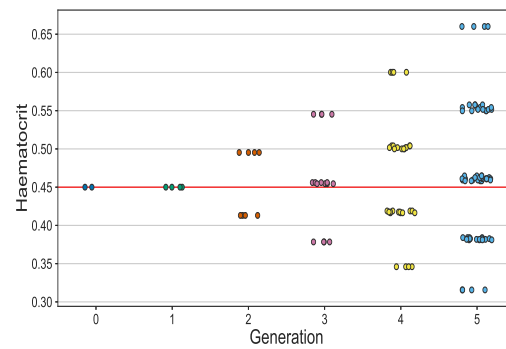
(a) A typical forking vessel network

(b) Vessel flow rates (in m^3/s)

(c) Distribution of haematocrit across vessel network (model with memory effects)

(d) Propagation of memory effects

Figure S4: (a) A typical symmetric forking network with 6 generations of vessels. (b) Flow rates almost halve between consecutive vessel generations. However, small differences in flow rates between daughter vessels arise due to non-uniform haematocrit splitting, as can be observed in inset (note that the range of the colour bar has been adjusted to represent only the selected vessels). (c) Differences in the predicted haematocrit levels of daughter vessels (within a single vessel generation) become more pronounced as the generation number increases. (d) For the new HS model, the haematocrit distribution becomes more disperse as the number of bifurcations included in the network increases (the red horizontal line represents the predicted haematocrit when memory effects are neglected and haematocrit is distributed uniformly across the network). Each circle corresponds to a single vessel and different colours correspond to different vessel generations.

21
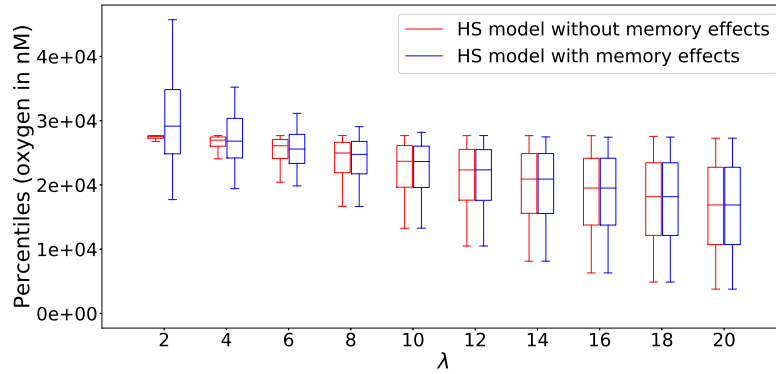
(a) Boxplots showing tissue oxygen concentration distribution as a function of λ
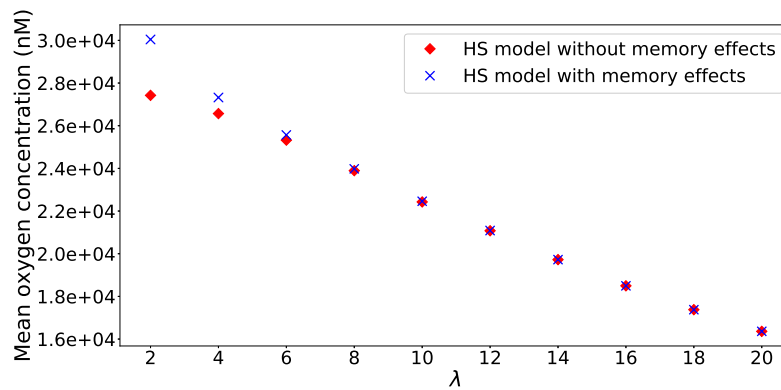
(b) Mean oxygen concentration as a function of λ
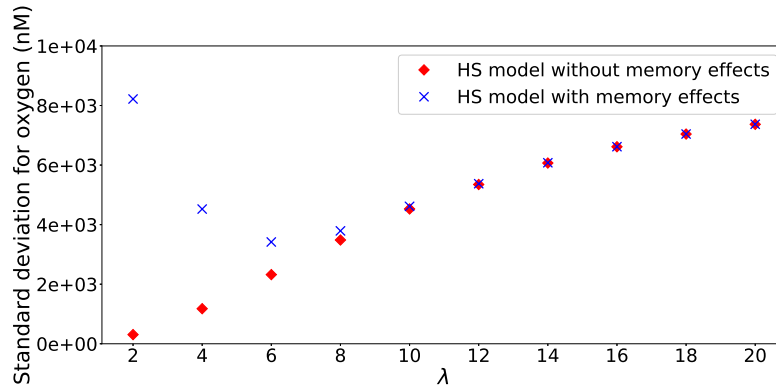
(c) Standard deviation (oxygen) as a function of λ

Figure S5: Summary statistics illustrating how for a vessel network with 6 generations its λ value and the HS model affect tissue oxygenation. a) Boxplots showing how the tissue oxygen distribution changes as λ varies for the two different HS rules. b) Mean oxygen concentration increases as λ decreases (and the vessel density increases). c) Standard deviation in the tissue oxygen concentration increases with λ when memory effects are neglected (Equation (1)). When memory effects are considered (Equation (2)), the standard deviation increases for small λ values. The mean and standard deviation for the two models converge for large λ values. Model parameter values as per Supplementary Table S4.
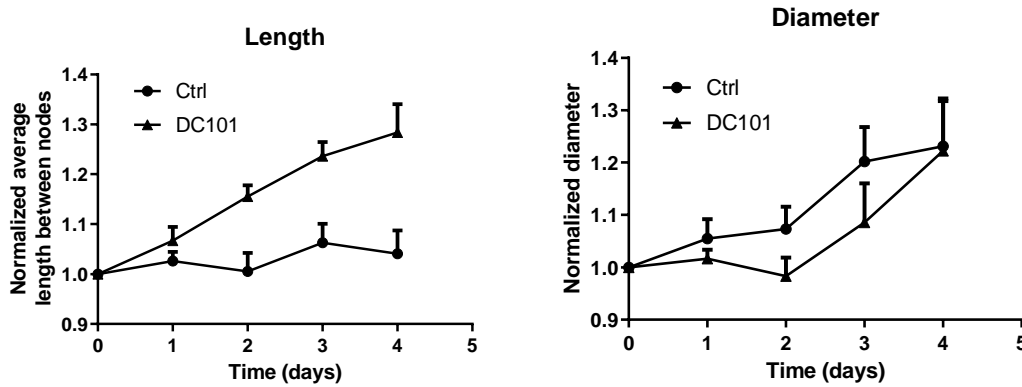
22

Figure S6: Vessel length and diameter in MC38 tumours over time following DC101 treatment compared with control (n=5).

A.1 Vessel lengths and diameters in tumour microvasculature are uncorrelated

In Supplementary Tables S2 and S3 we list Pearson's r-values quantifying the correlation between vessel lengths, L, and diameters, d,

$$\rho_{L,d} = \frac{\text{cov}(L,d)}{\sigma_L \sigma_d} \ , \tag{S.1}$$

where $\text{cov}(i,j)$ is the covariance of two variables and σ_i is the standard deviation of variable i, for the three tumour cell lines used in our experiments. Results are presented for each mouse and each scan. Day 0 was chosen as the day when the tumour vascular network appeared to be fully formed. This normally occurred about 8 days after tumour induction, when the tumour size was approximately 4mm in diameter. We note also that the duration of the observation period is cell-line specific; some tumours grew faster than others and soon started pushing on the window thus the animal had to be culled as per licence limitations. The Pearson's r-values are too low to conclude that a correlation exists between L and d in the tumour vascular networks studied.

A.2 Red blood cell suspension model

LBM numerically approximates the solution of the Navier-Stokes equations for a weakly compressible Newtonian fluid discretised on a regular lattice. We employ the D3Q19 lattice, the Bhatnagar–Gross–Krook collision operator extended with the Guo forcing scheme [66], the Bouzidi-Firdaouss-Lallemand (BFL) implementation of the no-slip boundary condition at the walls [67], and the Ladd implementation of the velocity boundary condition for open boundaries [68]. All these methods have been extensively used and analysed in the literature (see [69, 70] for a complete presentation).

The RBC membrane is modelled as a hyperelastic, isotropic and homogeneous material, following the model described in [43]. The different contributions to the total membrane energy W is given by $W = W^S + W^B + W^A + W^V$, where the superscripts denote strain, bending, area and volume. We employ the surface strain energy density

Table S2: Timecourse of Pearson's r-values calculated for different mice at different days of measurement implanted with the MC38 cell line. Day 0 corresponds to the day of the first measurement, when the tumour reached a specified size (4mm in diameter; see the main text). The corresponding values of $\bar{L}$, $\bar{d}$ and λ are reported in the main text (see Table 1). The missing datum for tumour 3 on Day 3 is due to the laser on the microscope failing during imaging.

Day	1	2	3	4	5	6
0	0.05	-0.06	-0.07	0.10	-0.13	0.00
1	0.03	-0.05	-0.07	-0.07	-0.13	-0.00
2	-0.08	-0.07	-0.06	-0.17	-0.19	0.02
3	-0.09	-0.09	-	-0.14	-0.13	-0.02
4	-0.14	-0.11	-0.08	-0.17	-0.12	-0.07
5	-	-0.09	-	-	-0.07	-0.11
6	-	-0.04	-	-	-	-
7	-	-0.08	-	-	-	-

Table S3: Timecourse of Pearson's r-values for mice implanted with the B16F10 and LLC cell lines. Day 0 corresponds to the day of the first measurement, when the tumour reached a specified size (4mm in diameter; see the main text). The corresponding values of $\bar{L}$, $\bar{d}$ and λ are reported in the main text (see Table 1).

	B16F10			LLC
Day	1	2	3	
0	-0.08	-0.08	-0.06	0.03
1	-0.05	-0.06	-0.09	0.02
2	-0.05	-0.12	-0.06	-
3	-0.03	-0.11	-0.06	-
4	-	-	-0.06	-
5	-	-	-0.05	-

24

w^S proposed by Skalak *et al.* [71]:

$$w^S = \frac{\kappa_s}{12} \left(I_1^2 + 2I_1 - 2I_2 \right) + \frac{\kappa_\alpha}{12} I_2^2 \ , \tag{S.2}$$

$$I_1 = \lambda_1^2 + \lambda_2^2 - 2 \ , \tag{S.3}$$

$$I_2 = \lambda_1^2 \lambda_2^2 - 1 \ , \tag{S.4}$$

where κ_s and κ_α are the shear and dilation moduli, λ_1, λ_2 are the local principal in-plane stretch ratios, and $W^S = \int dA\, w^S$. The shape of the discocyte membrane is approximated by a number N_f of flat triangular faces, and W^S is numerically calculated based on an FEM approach as

$$W^S = \sum_{j=1}^{N_f} A_j^{(0)} w_j^s \ , \tag{S.5}$$

where $A_j^{(0)}$ is the undeformed area of face j. The bending energy of the RBC membrane is numerically calculated as

$$W^B = \sqrt{3} \kappa_B \sum_{\langle i,j \rangle} \left(\theta_{i,j} - \theta_{i,j}^{(0)} \right)^2 \ , \tag{S.6}$$

where κ_B is the bending modulus, $\theta_{i,j}$ is the angle between the normals of two neighbouring faces i and j, and $\theta_{i,j}^{(0)}$ is the same angle for the undeformed membrane. Finally, we penalise deviations of the total membrane surface area and volume by defining two additional energy contributions:

$$W^A = \frac{\kappa_A}{2} \frac{\left(A - A^{(0)} \right)^2}{A^{(0)}} \ , \tag{S.7}$$

$$W^V = \frac{\kappa_V}{2} \frac{\left(V - V^{(0)} \right)^2}{V^{(0)}} \ , \tag{S.8}$$

where κ_A, κ_V are the surface area and volume moduli, A and $A^{(0)}$ are the current and undeformed membrane surface areas, and similarly with V. The principle of virtual work yields the force acting on each membrane vertex i at position $\mathbf{x}_i$ through

$$\mathbf{F}_i = -\frac{\partial W(\{\mathbf{x}_i\})}{\partial \mathbf{x}_i}. \tag{S.9}$$

The immersed boundary method [72] is used to couple fluid and membrane dynamics. The fluid velocity is interpolated at the positions $\mathbf{x}_i$ of the RBC mesh vertices, and a forward-Euler scheme is used to advect the vertices to satisfy the no-slip condition. The vertex forces $\mathbf{F}_i$ are spread to the lattice where they are used as input to the forcing term in the LBM, which ensures local momentum exchange between the membrane and the fluid. See [43] for a detailed numerical analysis of the algorithm.

A.3 CFL width calculation

To calculate the CFL width in channel 1 of the domains in Supplementary Figure S1, let us consider a vessel cross-section of diameter d at distance l downstream from the first bifurcation in the network. The RBC density, $\phi(r, \theta, l, t)$, is 1 if there is a RBC at time t occupying the point with radial coordinate r and angular coordinate θ of the cross-section and 0 otherwise. The average RBC density flux $\Phi(l)$ going through the cross-section is

$$\Phi(l) = \frac{1}{N} \sum_{i=1}^{N} \int_0^{2\pi} d\theta \int_0^{d/2} r dr \phi(r, \theta, l, t_i) \mathbf{v}(r, \theta, l, t_i) \cdot \mathbf{n} ,$$

where $\mathbf{v}$ is the fluid velocity, $\mathbf{n}$ is the cross-section normal vector and N is the number of simulation time steps in the average (0.5 s of real time simulation sampled every 0.0215 s, $N = 23$, in our case).

We define $\chi = 0.01$ as the average fraction of RBC density flux crossing the CFL. Now we are able to numerically determine the local CFL width $W(l, \theta)$: consider a 2D-cone centered and contained in the cross-section with orientation θ and size $\Delta\theta = \pi/2$. The width $W(l, \theta)$ is the distance such that

$$\chi = \frac{4}{\Phi N} \sum_{i=1}^{N} \int_{\theta-\Delta\theta/2}^{\theta+\Delta\theta/2} d\theta' \int_{d/2-W}^{d/2} r dr \phi(r, \theta', l, t_i) \mathbf{v}(r, \theta', l, t_i) \cdot \mathbf{n} .$$

Since we are only interested in the spatial evolution of the CFL, the specific value of χ used in the definition is arbitrary. The choice of χ will change the width of the CFL after symmetry recovery, but it will not affect the local characterisation of the CFL spatial evolution after a bifurcation. For example, for any value of χ, the CFL recovery distance can be calculated as the shortest distance l for which the CFL width W do not depend on coordinate θ.

A.4 Hybrid model of oxygen transport in vascularised tissue

A.4.1 Choice of vessel diameters and branching angles in vascular networks

In the branched networks used in Section 2.3, we fix the diameter of the inlet vessel so that $d_{inlet} = 100\ \mu$m. The diameters of the two daughter vessels (d_α and d_β) are assumed to be equal and determined from the parent vessel diameter (d_P) via Murray's law [47] so that:

$$d_P^3 = d_\alpha^3 + d_\beta^3 = 2d_\alpha^3,$$

which means that

$$d_\alpha = \frac{d_P}{2^{\frac{1}{3}}}.$$

The network is symmetric about its central axis and so vessels on the converging side of the network have the same diameter as those of the same generation on the diverging side; see Supplementary Figure S4a. For all simulations the networks have 6 generations of vessels. The length L of a vessel segment in a given network is related to its diameter d via $L = \lambda d$.

For complete specification of the network geometry, in two-dimensional cartesian geometry it remains to embed the network in a spatial domain. This is achieved by specifying

26

either the branching angles, or (equivalently) the lengths of the projections of the vessels on the y axis. Denoting by L_1^{vert} the length of the projection of a vessel of generation 1, the lengths of the projection of vessels of generation $i > 1$ are given by $L_i^{vert} = \frac{1}{2}L_{i-1}^{vert}$. As a result, the vertical size of the domain will not exceed $4L_1^{vert}$ for any number of generations. Finally, we require $L_1^{vert} < L_1 =$ length of vessels of generation 1. In our simulations, we fix $L_1^{vert} = 0.9L_1$ to ensure adequate spatial extent in the $y-$ direction.

A.4.2 Poiseuille's law and Fahraeus-Lindquist effect

We simulate flow in the branched networks by following the approach of Pries *et al.* [65]. For blood vessels of length L and diameter d, we assume Poiseuille's law

$$Q = \frac{\pi}{128}\frac{\Delta p d^4}{L\mu}, \tag{S.10}$$

where Q is the vessel flow rate, Δp is the pressure drop along the vessel and μ is the viscosity of blood [64]. Following [73] we assume that the blood viscosity depends on vessel diameter and haematocrit via the empirical relationship:

$$\mu = \mu_p\left[1 + (\mu_{45} - 1)\frac{(1-H)^C - 1}{(1-0.45)^C - 1}\left(\frac{d}{d-1.1}\right)^2\right]\left[\frac{d}{d-1.1}\right]^2,$$

where μ_p is the plasma viscosity, H is the vessel haematocrit,

$$\mu_{45} = 6e^{-0.085d} + 3.2 - 2.44e^{-0.06d^{0.645}}$$

and

$$C = \left(0.8 + e^{-0.075d}\right)\left(-1 + \frac{1}{1+10^{-11}d^{12}}\right) + \frac{1}{1+10^{-11}d^{12}}.$$

Introducing signed flow rates $\tilde{Q}_i$ for the sake of brevity, we impose the conservation of blood and haematocrit at each network bifurcation, so that

$$\sum_i \tilde{Q}_i = 0, \tag{S.11}$$

and

$$\sum_i \tilde{Q}_i H_i = 0. \tag{S.12}$$

In Equations (S.11) and (S.12) we sum over the three vessels that meet at that bifurcation. At diverging bifurcations, we impose a HS rule: we use Equation (1) when CFL memory effects are neglected and Equation (2) when they are included. Denoting by N_B the number of network bifurcations and N_V the number of vessels, we have N_B unknown pressures P, N_V unknown flow rates Q and $N_V - 1$ unknown haematocrit levels (the inlet haematocrit being prescribed) - altogether $N_B + 2N_V - 1$ unknowns. At the same time, we impose Poiseuille's law (S.10) for every vessel (N_V times), conservation of blood (S.11) and haematocrit (S.12) at every bifurcation node (N_B times), and an HS rule at all diverging bifurcations ($N_B/2$ times), yielding a total of $N_V + 5N_B/2$ algebraic equations. Since every bifurcation connects 3 vessels, we have $N_V = (3N_B + 2)/2$, where every vessel is counted twice, except for the inlet and outlet vessels ($+2$ in the numerator). From this, it follows that the number of equations ($N_V + 5N_B/2$) equals the number of unknowns ($N_B + 2N_V - 1$).

A.4.3 Oxygen distribution in tissue

In this section, we determine the oxygen concentration c in the tissue. Following [23], we assume that the dominant processes governing its distribution are delivery from the vessel network, diffusive transport through the tissue and consumption by cells in the tissue. We focus on the long time behaviour and therefore adopt a quasi-steady state approximation

$$\underbrace{D\nabla^2 c}_{\text{diffusive transport through the tissue}} + \underbrace{\pi d_l \gamma \left(\frac{\beta_{ref}}{H_{ref}} H_l - c \right) \delta_{network}}_{\text{delivery from the blood vessels}} - \underbrace{\kappa c}_{\text{consumption by the tissue}} = 0 \ .$$

(S.13)

In Equation (S.13), the positive constants D, γ and κ represent the diffusion coefficient for oxygen in the tissue, the vessel permeability to oxygen and the rate at which it is consumed by the cells in the tissue. The vessel network is represented by a collection of Dirac point sources $\delta_{network}$ where

$$\delta_{network}(\boldsymbol{x}) = \begin{cases} 1 & \text{if vessel is located at } \boldsymbol{x} \\ 0 & \text{otherwise} \end{cases}$$

and for any $\boldsymbol{x}$ satisfying $\delta_{network}(\boldsymbol{x}) = 1$, d_l and H_l are the diameter and haematocrit of the vessel at that location (where the latter has been calculated as described in the previous section). The constant β_{ref} represents the oxygen concentration of a reference vessel containing haematocrit H_{ref} (here we fix $H_{ref} = 0.45$, the inlet haematocrit) and we suppose that the oxygen concentration of a vessel with haematocrit H_l is $\beta_{ref} H_l / H_{ref}$. In Equation (S.13) we assume that the oxygen is supplied by vessels to the tissue at a rate which is proportional to their circumference πd_l, the vessel permeability γ, and $\beta_{ref} H_l / H_{ref} - c$. Finally, we have $\beta_{ref} = c_{stp} p_{ref} \alpha_{eff}$, where c_{stp} denotes an ideal gas concentration at standard temperature and pressure, p_{ref} denotes the reference partial pressure at the inlet vessel, and α_{eff} denotes the volumetric oxygen solubility [74]. A summary of the parameter values used to solve Equation (S.13) is presented in Supplementary Table S4.

A.5 Derivation of and justification for the HS model with CFL memory

A.5.1 Parameter dependencies in HS model without memory from [45]

The dependencies of the parameters A, B and X_0 (discussed in Section 4.3.2; see Equation (1)) on the diameters of the parent and both daughter vessels (d_P, d_α and d_β, respectively), and the discharge haematocrit H_P in the parent vessel were first introduced in [65] and later adjusted in [45] to achieve a better approximation under extreme combinations of d_α, d_β, d_P and H_P. We will use the functional forms from [45], which read

$$A = -13.29 \left[\left(d_\alpha^2 / d_\beta^2 - 1 \right) / \left(d_\alpha^2 / d_\beta^2 + 1 \right) \right] \left(1 - H_P \right) / d_P, \tag{S.14}$$

$$B = 1 + 6.98 \left(\frac{1 - H_P}{d_P} \right) \tag{S.15}$$

Table S4: Parameters used to simulate tissue oxygen.

Parameter	Description	Value	Unit	Reference
D	Diffusivity	0.00145	$\mathrm{cm}^2\ \mathrm{min}^{-1}$	[75]
κ	Consumption rate	13.0	min^{-1}	[75]
γ	Vessel permeability	6.0	$\mathrm{cm}\ \mathrm{min}^{-1}$	[75]
c_{stp}	See Section A.4.3	$\frac{1}{0.0224}$	$\mathrm{mol}\ \mathrm{m}^{-3}$	[76]
p_{ref}	Reference partial pressure	20	mmHg	[75]
α_{eff}	Volumetric solubility	3.1×10^{-5}	mmHg^{-1}	[74]
H_{inlet}	Inlet haematocrit	0.45	-	[77]
d_{inlet}	Diameter of inlet vessel	100	μm	Estimated from [64]
A_{shift}	See Section A.5.2	0.5	-	Estimated Sec. A.5.2
ω	See Section A.5.2	4	-	Estimated Sec. A.5.2
μ_p	Plasma viscosity	10^{-3}	Poiseuille	Similar to [75]
p_{in}	Inlet pressure	3.32×10^3	Pa	Similar to [75]
p_{out}	Outlet pressure	2.09×10^3	Pa	Similar to [75]

and

$$X_0 = 0.964(1 - H_P)/d_P. \tag{S.16}$$

These functional forms assume that d_P is without units (given in microns). We will stick to this convention throughout this section.

A.5.2 HS model with memory

Simplifying assumptions. Before we discuss the further details of the newly-developed extension to the model from [45] incorporating the memory effects in detail, we briefly comment on its main simplifying assumptions. Our model at the moment does not include any information on local flow rate (apart from information on the distance to the previous bifurcation) and a more realistic model for the CFL recovery should include such information. Furthermore, the current model is two-dimensional. However, these simplifying assumptions could easily be relaxed in future work. For instance, in three dimensions, one needs to consider information on the angle defined by the planes containing the current and previous bifurcation in the model. Therefore, the model presented here should be regarded as a first attempt to account for CFL disruption effects in HS.

Rewriting of the model. In this section, we rewrite the HS model with memory effects given in terms of the fractional blood (FQ_B) and erythrocyte (FQ_E) flow rates (Equation (2)) so that it is expressed in terms of haematocrit levels H and flow rates Q experienced by the vessels belonging to a given bifurcation (Equation (3)). The definitions of $FQ_{E,f}$ and $FQ_{B,f}$ can be mathematically written as:

$$FQ_{E,f} = \frac{Q_f H_f}{Q_P H_P}, \qquad FQ_{B,f} = \frac{Q_f}{Q_P}.$$

Substituting these expressions into Equation (2) from the main text gives:

$$\mathrm{logit}\left(\frac{Q_f H_f}{Q_P H_P}\right) = A_f + B\,\mathrm{logit}\left(\frac{Q_f/Q_P - X_{0,f}}{1 - X_{0,u} - X_{0,f}}\right),$$

and recalling that $\text{logit}(x) = \ln\left(x/(1-x)\right)$, we have

$$\ln\left(\frac{Q_f H_f}{Q_P H_P - Q_f H_f}\right) = A_f + B\,\ln\left(\frac{Q_f - X_{0,f}Q_P}{Q_P - Q_f - X_{0,u}Q_P}\right).$$

Using the conservation of blood (overall)

$$Q_P = Q_f + Q_u$$

and RBCs (in particular)

$$Q_P H_P = Q_f H_f + Q_u H_u \tag{S.17}$$

at diverging bifurcations, we arrive at

$$\ln\left(\frac{Q_f H_f}{Q_u H_u}\right) = A_f + B\,\ln\left(\frac{Q_f - X_{0,f}Q_P}{Q_u - X_{0,u}Q_P}\right).$$

This can also be written as

$$\ln\left(\frac{H_f}{H_u}\right) = A_f + B\,\ln\left(\frac{Q_f - X_{0,f}Q_P}{Q_u - X_{0,u}Q_P}\right) - \ln\left(\frac{Q_f}{Q_u}\right),$$

which yields

$$\frac{H_f}{H_u} = e^{A_f} \times \left(\frac{Q_f - X_{0,f}Q_P}{Q_u - X_{0,u}Q_P}\right)^B \times \frac{Q_u}{Q_f}.$$

Choice of parameters and CFL recovery function. Now we introduce the functional forms for A_f, $X_{0,f}$ and $X_{0,u}$, using empirical data to justify our choices. Guided by the dependence of A on the branching history of the network described in [16] (see Figure 7 therein), we propose

$$A_f = A + A_{shift} f(l; d_P), \tag{S.18}$$

where A is given in (S.14), the positive constant A_{shift} corresponds to the maximum CFL disruption effect, and the function $f(l; d_P)$ describes how the recovery of the CFL depends on the distance l to the previous bifurcation and the diameter d_P of the parent vessel[3].

For parameter A, we only have access to the scattered data with respect to the regressor from [65] (as opposed to the regressor from [45]), which reads

$$A = -6.96 \ln\left(\frac{d_\alpha}{d_\beta}\right)/d_P \tag{S.19}$$

and using the extreme values of A in these data (see Supplementary Figure S7c), we estimate $A_{shift} = 0.5$. Note that in branching networks with every pair of daughter vessels having equal radii (as is the case in Section 4.3), both [65] and [45] yield $A = 0$. Thus, for our networks, the choice of A does not affect A_f at all (see Equation (S.18)).

---

[3]Consistency of the model requires that $A_u = A - A_{shift}f(l; d_P)$.

Table S5: Haematocrits predicted by the model with CFL memory effects

Distance	H_{inlet}	H_u	H_f
$\delta = 4d$	20.0	17.7	22.3
$\delta = 11d$	20.0	19.6	20.4
$\delta = 18d$	20.0	19.9	20.1
$\delta = 25d$	20.0	20.0	20.0

For simplicity, we model the CFL recovery using an exponential function

$$f(l; d_P) = e^{-\frac{l}{\omega d_P}} \ , \tag{S.20}$$

where ω controls the temporal dynamics of CFL recovery. From [42], we note that the CFL width is (approximately) 90% recovered at a distance $l_{90} = 10 d_P$ from the previous bifurcation (see also Figure 2g). Accordingly, we choose ω so that

$$0.1 = e^{-\frac{10}{\omega}} \implies \omega = \frac{10}{\ln(10)} \approx 4.$$

Guided by the dependence of $X_{0,f}$ on flow history described in [16], we propose

$$X_{0,f} = X_0 \left(1 - f(l; d_P)\right). \tag{S.21}$$

Assuming, as a first approximation, that $X_{0,f} + X_{0,u}$ is constant and independent of the distance to the previous bifurcation (see Figure 2g), we define

$$X_{0,u} = X_0 \left(1 + f(l; d_P)\right). \tag{S.22}$$

### A.5.3 Validation of the HS model with memory

We validate the HS model with memory by comparing its predictions with results from the RBC simulations in the double-t geometry in Section 2.2. We assume that all vessels have the same diameter ($d = 33\ \mu$m), and that the flow rate splits evenly at both bifurcations. If we assume further that the CFL is fully established at the network inlet vessel, $H_{inlet} = 20\%$, then Equation (1) supplies $H_1 = H_2 = H_{inlet} = 20\%$. We use conservation of RBCs (S.17) and the new HS model (3) to estimate haematocrit values in the unfavourable and favourable daughter branches after the second bifurcation (channels 3 and 4, respectively) for varying inter-bifurcation distances δ. The results are summarised in Supplementary Table S5. For $\delta = 4d$, the new HS model predicts haematocrits within 5% of the values calculated from RBC simulations in Section 2.2. Given the uncertainty in determining discharge haematocrit in the RBC simulations and given that the new model neglects effects due to asymmetric streamline splitting [44], we conclude that our new model provides a good leading-order approximation to the effect of CFL disruption on HS.

Finally, we compare the CFL evolution dynamics calculated from the RBC simulations (for $\theta = 0$ and $\theta = \pi$) with those predicted from the proposed evolution of $X_{0,f}$ and $X_{0,u}$

31
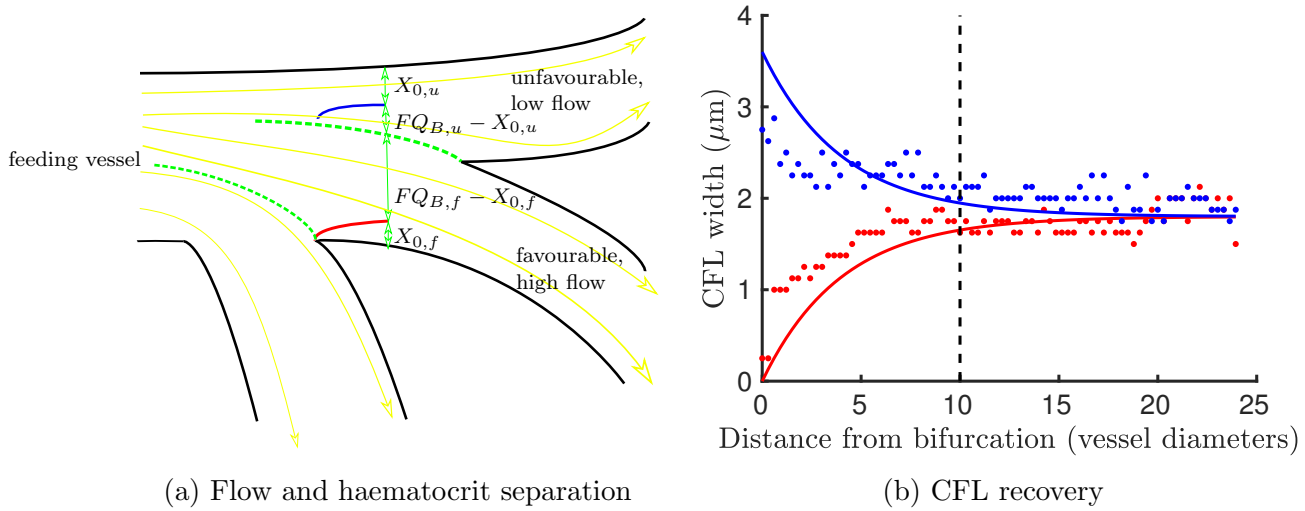
(a) Flow and haematocrit separation

(b) CFL recovery
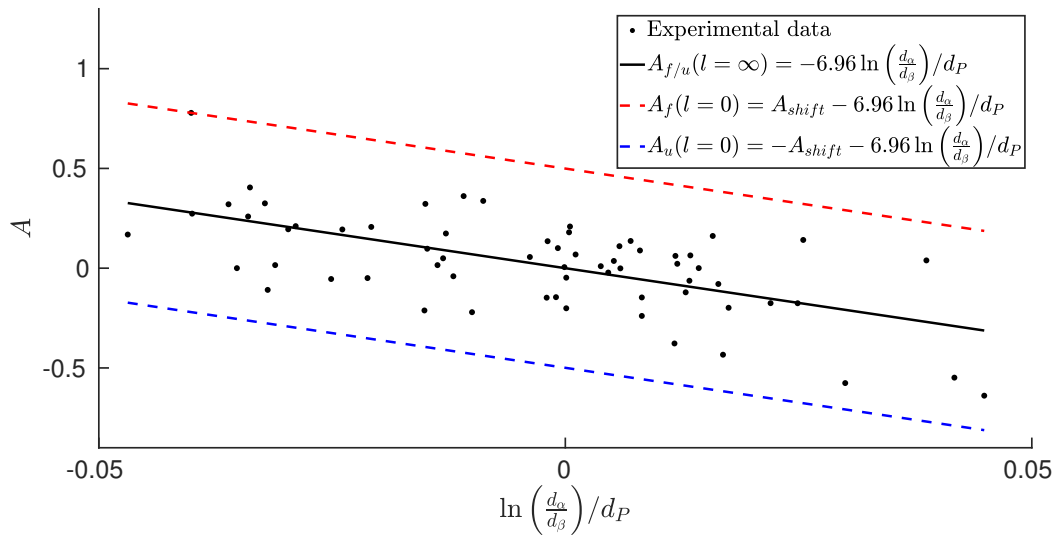
(c) Dispersion of data for A from [16]

Figure S7: (a) A schematic diagram presenting the geometric intuition behind (blood) flow and haematocrit separation helps us understand the need for two distinct minimum-flow fractions for the favourable and the unfavourable branches. Blood flow separation at the two consecutive bifurcations is shown in dotted green, streamlines are sketched with yellow curved arrows, and the CFL recovery on the favourable (unfavourable) side of the parent vessel after the first bifurcation is sketched in red (blue). Whenever $FQ_{B,f} < X_{0,f}$ ($FQ_{B,u} < X_{0,u}$), the favourable (unfavourable) branch only draws blood from the CFL and it thus receives pure plasma. (b) Model of CFL recovery as described by Equation (S.25) shows similar trends to and is in satisfactory agreement with the CFL width data from RBC simulations in Figure 2g (given the simplifying assumptions). The established CFL width of 1.8 μm chosen by inspection for this particular dataset. (c) Dispersion of values for A (reproduced using Figure 6 from [16]) is used with the regression from [65] to estimate the value of $A_{shift} \approx 0.5$ in Equation (S.18), based on deviation from the regression. We assume the CFL disruption to be the primarily cause of this deviation, and thus its maximum (absolute) value should correspond to $l = 0$ in (S.20) (i.e. $f = 1$ in (S.18)).

32

(Equations (S.21) and (S.22)). In the absence of a known functional form relating the CFL width W and the minimum flow fraction X_0, we define

$$X_{0,f/u} = \frac{W_{f/u}}{d_P}. \tag{S.23}$$

Equation (S.23) is based on the diagram in Supplementary Figure S7a and the assumptions of a cross-sectionally uniform velocity profile within a one-dimensional vessel cross-section. Combining (S.16), (S.23), (S.21) and (S.22), we conclude

$$W_{f/u} = d_P X_{0,f/u} = d_P X_0 \left(1 \mp f(l, d_P)\right) = 0.964 \times (1 - H_P) \left(1 \mp e^{-\frac{l}{4 \times d_P}}\right). \tag{S.24}$$

We remark that for a well-established CFL (i.e. $l \to \infty$), Equation (S.24) predicts (noting that channel 1 serves as the parent vessel for the second bifurcation and concluding the value $H_P = 0.2$ from Table 5) a CFL width of about 0.77 μm, whereas our RBC simulation predicts a value of approximately 1.8 μm (see Supplementary Figure S7b). We postulate that this discrepancy is caused by our oversimplification of the relationship between the CFL width and the minimum flow fraction (Equation (S.23)). Nevertheless, we can adjust Equation (S.24) so that it is consistent with the established CFL width of 1.8 μm by writing

$$W_{f/u} = 1.8 \times \left(1 \mp e^{-\frac{l}{4 \times d_P}}\right). \tag{S.25}$$

In this case the CFL evolution (for $\theta = 0$ and $\theta = \pi$) follows a trend similar to that observed in our RBC simulations (Supplementary Figure S7b). In particular, our assumption that $l_{90} = 10 d_P$ is in good agreement with our simulation results (see dashed line in Supplementary Figure S7b).

A.6 Explanation of higher mean oxygen values for small λ

In Section 2.3, we observed that CFL-disruption effects increase the mean oxygen concentration in the chosen network. Here, we provide an explanation of this phenomenon.

We define

$$\Delta_\alpha H = H_\alpha - H_P, \quad \Delta_\beta H = H_\beta - H_P, \tag{S.26}$$

where P is the parent branch and α and β are the daughter branches of any diverging bifurcation. Conservation of blood and RBCs at this bifurcation then yields

$$Q_\alpha + Q_\beta = Q_P \tag{S.27}$$

$$Q_\alpha (H_P + \Delta_\alpha H) + Q_\beta (H_P + \Delta_\beta H) = Q_P H_P. \tag{S.28}$$

Combining (S.28) and (S.27) supplies

$$\frac{Q_\alpha}{Q_\beta} = -\frac{\Delta_\beta H}{\Delta_\alpha H}. \tag{S.29}$$

We deduce that, at diverging bifurcations, the haematocrit level in the daughter branch with higher flow rate deviates less (in absolute value) from the haematocrit in the parent vessel than the branch with lower flow rate.

We note further that all paths connecting the inlet and outlet vessels in the direction of blood flow in a given network are topologically and geometrically equivalent. Therefore, heterogeneity in haematocrit splitting arises solely from CFL-disruption effects. If haematocrit is elevated in one of the daughter branches, its impedance will increase, and, as a result, it will receive a lower flow rate.

Combining these two effects, we see that, in the chosen networks, haemoconcentration in any daughter branch is more significant than haemodilution in its sibling. As a consequence, and given that the strength of the oxygen source term in Equation (S.13) is a linear function of H, we observe higher mean oxygen levels when the effects of CFL disruption are taken into account (especially for small λ). Future work will investigate this effect by making source term a function of RBC mass flux (*i.e. QH*) or relaxing the assumption that the RBCs have infinite oxygen carrying capacity.

References

[1] J. A. Bertout, S. A. Patel, M. C. Simon, *Nature Reviews Cancer* **8**, 967 (2008).

[2] L. H. Gray, A. D. Conger, M. Ebert, S. Hornsey, O. C. A. Scott, *The British Journal of Radiology* **26**, 638 (1953).

[3] N. S. Vasudev, A. R. Reynolds, *Angiogenesis* **17**, 471 (2014).

[4] A. L. Harris, *Nature Reviews Cancer* **2**, 38 (2002).

[5] D. R. Grimes, *et al.*, *Journal of The Royal Society Interface* **13** (2016).

[6] R. K. Jain, *Science* **307**, 58 (2005).

[7] R. K. Jain, *Nature Medicine* **7**, 987 (2001).

[8] T. T. Batchelor, *et al.*, *Proceedings of the National Academy of Sciences* **110**, 19059 (2013).

[9] S. M. Bentzen, V. Gregoire, Molecular Imaging-Based Dose Painting: A Novel Paradigm for Radiation Therapy Prescription (2011).

[10] M. Skórska, T. Piotrowski, *Reports of Practical Oncology & Radiotherapy* **22**, 327 (2017).

[11] D. R. Grimes, D. R. Warren, S. Warren, *British Journal of Radiology* **90** (2017).

[12] J. Scott, A. Marusyk, *Biochimica et Biophysica Acta - Reviews on Cancer* **1867**, 139 (2017).

[13] A. S. Popel, *Crit Re v Biomed Eng* **293**, H3740 (1989).

[14] K. Svanes, B. W. Zweifach, *Microvascular Research* **1**, 210 (1968).

[15] Y. C. Fung, *Microvascular Research* **5**, 34 (1973).

[16] A. Pries, K. Ley, M. Claassen, P. Gaehtgens, *Microvascular Research* **38**, 81 (1989).

[17] V. Doyeux, T. Podgorski, S. Peponas, M. Ismail, G. Coupier, *Journal of Fluid Mechanics* **674**, 359 (2011).

[18] Y. C. Fung, *Biomechanics : Circulation* (Springer New York, 1997).

[19] I. G. Gould, A. A. Linninger, *Microcirculation* **22**, 1 (2015).

[20] D. Ribatti, B. Nico, E. Crivellato, A. Vacca, *Cancer Letters* **248**, 18 (2007).

[21] W. S. Kamoun, *et al.*, *Nature methods* **7**, 655 (2010).

[22] G. Helmlinger, F. Yuan, M. Dellian, R. K. Jain, *Nature Medicine* **3**, 177 (1997).

[23] J. A. Grogan, *et al.*, *Biophysical Journal* **112**, 1767 (2017).

[24] L. Hlatky, *CancerSpectrum Knowledge Environment* **94**, 883 (2002).

[25] A. Daşu, I. Toma-Daşu, M. Karlsson, *Acta Oncologica* **44**, 563 (2005).

[26] J. G. Scott, A. G. Fletcher, A. R. Anderson, P. K. Maini, *PLoS Computational Biology* **12**, 1 (2016).

[27] J. A. Grogan, *et al.*, *IEEE Transactions on Biomedical Engineering* **PP** (2016).

[28] L. Ritsma, *et al.*, *Nature Protocols* **8**, 583 (2013).

[29] R. Bates, *et al.*, *IEEE Transactions on Medical Imaging* pp. 1–10 (2017).

[30] R. Bates, *et al.*, *arXiv:1705.09597* (2017).

[31] S. J. Chapman, R. J. Shipley, R. Jawad, *Bulletin of Mathematical Biology* **70**, 2334 (2008).

[32] B. R. Duling, I. H. Sarelius, W. F. Jackson, *International journal of microcirculation, clinical and experimental* **1**, 409 (1982).

[33] A. S. Popel, *Journal of Applied Mechanics* **47**, 247 (1980).

[34] M. P. Wiedeman, *Circulation Research* **10**, 686 (1962).

[35] M. P. Wiedeman, *Circulation Research* **12**, 375 (1963).

[36] A. Koller, B. Dawant, A. Liu, A. S. Popel, P. C. Johnson, *American Journal of Physiology-Heart and Circulatory Physiology* **253**, H154 (1987).

[37] S. D. House, P. C. Johnson, *American Journal of Physiology-Heart and Circulatory Physiology* **250**, H828 (1986).

[38] M. Ellsworth, A. Liu, B. Dawant, A. Popel, R. Pittman, *Microvascular Research* **34**, 168 (1987).

[39] A. R. Pries, T. W. Secomb, *Clinical hemorheology and microcirculation* **29**, 143 (2003).

[40] F. Yuan, *et al.*, *Cancer Research* **54**, 4564 (1994).

[41] O. Oulaid, J. Zhang, *Biomechanics and Modeling in Mechanobiology* **14**, 783 (2015).

[42] D. Katanov, G. Gompper, D. A. Fedosov, *Microvascular Research* **99**, 57 (2015).

[43] T. Krüger, *Computer simulation study of collective phenomena in dense suspensions of red blood cells under shear* (Springer Spektrum, 2012).

[44] Z. Wang, Y. Sui, A. V. Salsac, D. Barthès-Biesel, W. Wang, *Journal of Fluid Mechanics* **849**, 136 (2018).

[45] A. Pries, T. Secomb, *American Journal of Physiology- . . .* pp. 2657–2664 (2005).

[46] J. Yang, S. S. Yoo, T.-R. Lee, *Physical Review E* **95**, 040401 (2017).

[47] C. D. Murray, *Proceedings of the National Academy of Sciences* **12**, 207 (1926).

[48] W. S. Kamoun, *et al.*, *Journal of Clinical Oncology* **27**, 2542 (2009).

[49] Y. Izumi, L. Xu, E. di Tomaso, D. Fukumura, R. K. Jain, *Nature* **416**, 279 (2002).

[50] R. K. Jain, *et al.*, *Proceedings of the National Academy of Sciences of the United States of America* **95**, 10820 (1998).

[51] L. Primo, *et al.*, *Cancer Research* **70**, 5759 (2010).

[52] R. T. Tong, *et al.*, *Cancer Research* **64**, 3731 (2004).

[53] F. Yuan, *et al.*, *Proceedings of the National Academy of Sciences* **93**, 14765 (1996).

[54] S. Kim, R. L. Kong, A. S. Popel, M. Intaglietta, P. C. Johnson, *American journal of physiology. Heart and circulatory physiology* **293**, H1526 (2007).

[55] C. Michiels, C. Tellier, O. Feron, *BBA - Reviews on Cancer* **1866**, 76 (2016).

[56] T. Stylianopoulos, R. K. Jain, *Proceedings of the National Academy of Sciences* **110**, 18632 (2013).

[57] C. A. Franco, *et al.*, *PLOS Biology* **13**, e1002125 (2015).

[58] C. A. Franco, *et al.*, *eLife* **5** (2016).

[59] A.-C. Vion, *et al.*, *The Journal of Cell Biology* **217**, 1651 (2018).

[60] K. Bentley, S. Chakravartula, *Philosophical Transactions of the Royal Society B: Biological Sciences* **372**, 20150522 (2017).

[61] T. Krüger, F. Varnik, D. Raabe, *Computers & Mathematics with Applications* **61**, 3485 (2011).

[62] M. D. Mazzeo, P. V. Coveney, *Computer Physics Communications* **178**, 894 (2008).

[63] M. O. Bernabeu, *et al.*, *Journal of The Royal Society Interface* **11**, 20140543 (2014).

[64] T. W. Secomb, *Comprehensive Physiology* **6**, 975 (2016).

[65] A. R. Pries, T. W. Secomb, P. Gaehtgens, J. F. Gross, *Circulation research* **67**, 826 (1990).

[66] Z. Guo, C. Zheng, B. Shi, *Physical Review E - Statistical, Nonlinear, and Soft Matter Physics* **65**, 1 (2002).

[67] M. Bouzidi, M. Firdaouss, P. Lallemand, *Physics of Fluids* **13**, 3452 (2001).

[68] A. J. C. Ladd, *Journal of Fluid Mechanics* **271**, 285 (1994).

[69] C. K. Aidun, J. R. Clausen, *Annual Review of Fluid Mechanics* **42**, 439 (2010).

[70] T. Krüger, *et al.*, *The Lattice Boltzmann Method: Principles and Practice* (2017).

[71] R. Skalak, P. I. Branemark, *Science* **164**, 717 (1969).

[72] C. S. Peskin, *Acta Numerica*, A. Iserles, ed. (Cambridge University Press, Cambridge, 2002), vol. 11, pp. 479–518.

[73] A. R. Pries, *et al.*, *Circulation Research* **75**, 904 (1994).

[74] T. W. Secomb, R. Hsu, E. Y. H. Park, M. W. Dewhirst, *Annals of biomedical engineering* **32**, 1519 (2004).

[75] M. R. Owen, *et al.*, *Cancer Research* **71**, 2826 (2011).

[76] H. N. S. Michael J. Moran, *Fundamentals of Engineering Thermodynamics* (2006).

[77] A. R. Pries, T. W. Secomb, P. Gaehtgens, *Cardiovascular research* **32**, 654 (1996).